29. Seager, W. R. Low-angle gravity glide structures in the northern Virgin Mountains, Nevada and Arizona. *Geol. Soc. Am. Bull.* **81,** 1517–1538 (1970).
30. Ollier, C. D. & Pain, C. F. Active rising surficial gneiss domes in Papua New Guinea. *J. Geol. Soc. Aust.* **27,** 33–44 (1980).

Acknowledgements

We thank E. Davis for providing the heat flow probes used in this study; T. Lewis and A. Taylor for their help and expertise in acquiring and reducing heat flow measurements at sea; the Captain and crew of the RV *Maurice Ewing* for their efforts which led to a successful cruise; and R. Buck and S. Baldwin for comments and suggestions which improved the paper. This work was supported by the US National Science Foundation.

Correspondence and requests for materials should be addressed to F.M. (e-mail: martinez@soest.hawaii.edu).

The elastic constants of $MgSiO_3$ perovskite at pressures and temperatures of the Earth's mantle

Artem R. Oganov, John P. Brodholt & G. David Price

Department of Geological Sciences, University College London, Gower Street, London WC1E 6BT, UK

The temperature anomalies in the Earth's mantle associated with thermal convection[1] can be inferred from seismic tomography, provided that the elastic properties of mantle minerals are known as a function of temperature at mantle pressures. At present, however, such information is difficult to obtain directly through laboratory experiments. We have therefore taken advantage of recent advances in computer technology, and have performed finite-temperature *ab initio* molecular dynamics simulations[2,3] of the elastic properties of $MgSiO_3$ perovskite, the major mineral of the lower mantle, at relevant thermodynamic conditions. When combined with the results from tomographic images of the mantle, our results indicate that the lower mantle is either significantly anelastic[4] or compositionally heterogeneous on large scales[5]. We found the temperature contrast between the coldest and hottest regions of the mantle, at a given depth, to be about 800 K at 1,000 km, 1,500 K at 2,000 km, and possibly over 2,000 K at the core–mantle boundary.

Ab initio molecular dynamics, pioneered by Car and Parrinello[2], has made a substantial impact on modern planetary and materials sciences[6–8]. Advantages of this approach—which is computationally expensive—include the explicit account of the quantum nature of electronic structure and interatomic interactions, and the description of the intrinsic anharmonicity of lattice vibrations. This is the method of choice for simulating high-temperature phenomena that are significantly anharmonic, such as melting[8,9], ionic conductivity, displacive phase transitions, thermal expansion[10], and elastic properties. Calculations of elastic constants of materials using *ab initio* molecular dynamics can be done by one of two routes: (1) from fluctuations of stress or strain, or (2) from stress–strain relations, that is, from Hooke's law. Both routes require enormous computational efforts; very long runs are required by the first method, and in the second method, it is necessary to perform several independent simulations for different lattice strains that include the nonlinearity of stress–strain relations. Recent advances in computer technology and increased accessibility of supercomputers have now made such simulations possible.

Orthorhombic $MgSiO_3$ perovskite is an ideal subject for *ab initio* molecular dynamics simulations. When containing some Fe, it is the most abundant mineral in the Earth, comprising 60–100 vol.% of the lower mantle, and dominating many of its properties. The lower mantle comprises over 50% of the Earth's volume; extending between the depths of 670 km and 2,891 km, it is characterized by very high pressures (24–136 GPa) and temperatures, roughly between 2,000 K and 3,000 K, possibly rising to about 4,000 K (ref. 11). At these temperatures atomic motion is essentially classical and possibly significantly anharmonic, making it appropriate to use the molecular dynamics approach. A hypothetical cubic phase with superionic conductivity has been proposed as an explanation of the observed high electrical conductivity of the lower mantle[12,13]; molecular dynamics is the only currently viable way to simulate fast ionic conduction phenomena in solids. Our previous work[14] considered 'static' elastic constants (that is, the thermal motion of atoms was neglected), and used *ab initio* molecular dynamics to study the thermal expansivity and the thermal equation of state of $MgSiO_3$ perovskite—which was found to stay orthorhombic at lower-mantle temperatures. Here we perform *ab initio* molecular dynamics simulations of elastic constants of $MgSiO_3$ perovskite at lower-mantle conditions, taking full account of temperature. At this stage we consider only pure $MgSiO_3$ perovskite. The effects of the moderate Fe content, while potentially important for certain properties (such as shear modulus), are expected to be negligible for others—especially for the thermal expansion, bulk modulus, and derivatives (with respect to pressure and temperature) of the elastic moduli and seismic wave velocities, which are the main subject of this work.

Seismic tomography gives insight into the three-dimensional structure and dynamics of the Earth, but its quantitative interpretation requires knowledge of temperature variations of seismic wave

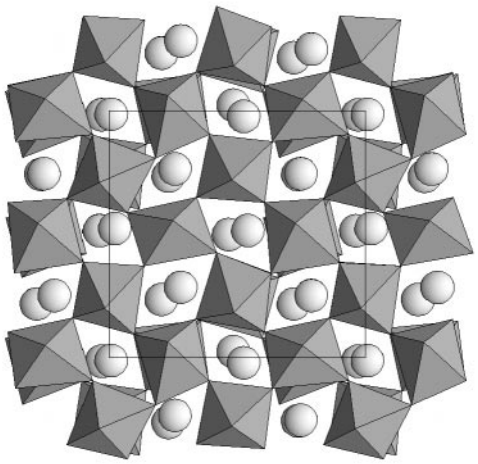

Figure 1 'Snapshot' of the crystal structure of $MgSiO_3$ perovskite from *ab initio* molecular dynamics simulations at 88 GPa and 3,500 K. The equilibrium structure at these conditions is orthorhombic. Spheres, Mg atoms; polyhedra SiO_6 octahedra. The supercell used in the calculations ($2a \times 2b \times 1c$ *Pbnm*-supercell, contours shown) contains 80 atoms. Simulations were also performed at 38 GPa and 1,500 K, 38 GPa and 2,500 K, 38 GPa and 3,500 K, 88 GPa and 1,500 K, and 136 GPa and 4,500 K, and at all conditions the optimized cell was orthorhombic. The simulated pressures of 38 GPa and 88 GPa correspond to depths of approximately 1,000 km and 2,000 km, respectively. Our simulations are based on density functional theory[23,24] within the generalized gradient approximation[25] and pseudopotential plane wave scheme. The pseudopotentials used are non-local, ultrasoft for O and norm-conserving with partial core corrections for Mg and Si. Plane-wave cut-off of 500 eV, which gives excellent convergence of all properties with respect to the basis set size, was used. Supercell periodicity was imposed on the wavefunction, which proved to give sufficiently accurate results with our large supercell. At each pressure/temperature condition, the simulations were run in the constant-*NVT* ensemble[26] for at least 0.79 ps after equilibration with 1 fs timestep. This was sufficient to produce accurate statistical averages of the stress tensor components. Cell dimensions were carefully optimized by making the stress tensor hydrostatic.

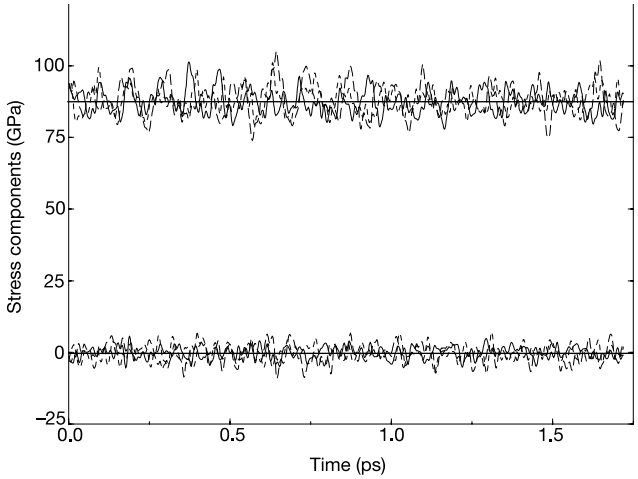

Figure 2 Fluctuations of the stress tensor components for the structure shown in Fig. 1. Data for the optimized cell at 88 GPa and 3,500 K show that the stress is hydrostatic. As the generalized gradient approximation often results in a shifted pressure scale[14], we corrected the calculated pressures and diagonal stress components by –12.08 GPa. This correction alters only the pressure scale, but not the properties. More information on the pressure correction and performance of the generalized gradient approximation can be found in ref. 14. Applying strains (we used one triclinic and three axial strains with magnitudes +0.02 and –0.02) and calculating the time-averages of the induced stresses, we calculated the isothermal elastic constants C_{ij} from nonlinear stress–strain relations; different elastic constants are obtained from different stresses. Adiabatic elastic constants, used in calculations of seismic velocities, were calculated from the isothermal constants[27] using the thermal pressure tensor calculated directly by *ab initio* molecular dynamics.

velocities. Seismology gives $R_T = (\partial \ln v_S / \partial \ln v_P)_T$, the ratio of variation of the shear (v_S) and compressional (v_P) velocities due to pressure alone, as 0.7 (ref. 1). A similarly defined parameter, $R_P = (\partial \ln v_S / \partial \ln v_P)_P$ measuring the same ratio, but due to temperature effects alone, is much larger: it increases from 1.7 to 2.6 between the depths of 1,000 km and 2,000 km according to seismic tomography data[15]. The large difference between R_T and R_P has been a puzzle for geophysicists over past 15 years; Anderson[1] suggested that the difference is entirely due to intrinsic anharmonicity, the simulation of which needs molecular dynamics or Monte Carlo methods, rather than the quasiharmonic approximation.

Our *ab initio* molecular dynamics simulations (Figs 1 and 2) were performed with the VASP code[3] run on 128 nodes of the CRAY T3E supercomputer at Manchester Computer Centre. The calculated equilibrium lattice parameters, isothermal and adiabatic elastic constants, and thermal expansion coefficients are presented in Table 1. One of the calculated points, 38 GPa and 3,500 K, is close to the melting point of $MgSiO_3$ perovskite[16] (results of this study indicated that melting would occur at ~3,800 K under a pressure of 38 GPa; however, there is still controversy about the melting curve of $MgSiO_3$ perovskite). Although we observed very large displacements of atoms, all atoms vibrated about their ideal crystallographic locations and did not diffuse, and shear elastic constants were large and positive. It is remarkable that even at these conditions orthorhombic $MgSiO_3$ perovskite does not transform to a cubic or tetragonal phase. Anomalous elastic constants obtained at these critical conditions were not used in the further analysis.

We calculate $R_T = 0.61$–0.81 (our static simulations[14] give 0.59–0.74), in keeping with geophysical observations. The value of R_P increases from 1.5 at a depth of 1,000 km to 1.9 at 2,000 km. These

Table 1 Properties of $MgSiO_3$ perovskite at high pressures and temperatures

	Conditions				
Property	38 GPa, 1,500 K	38 GPa, 2,500 K	38 GPa, 3,500 K	88 GPa, 1,500 K	88 GPa, 3,500 K
V	147.63	150.83	154.08	132.55	136.48
a	4.628	4.675	4.723	4.435	4.499
b	4.792	4.814	4.836	4.655	4.674
c	6.658	6.703	6.747	6.420	6.492
$\sigma_{1;2;3}$	37.9; 38.0; 37.9	38.0; 37.6; 37.3	37.0; 39.0; 38.0	88.1; 87.7; 88.4	87.8; 87.9; 88.5
P	37.9	37.6	38.0	88.1	88.1
$C_{11}^{T/S}$	601/616	553/579	525/564	813/826	749/783
$C_{22}^{T/S}$	697/711	629/654	545/578	978/991	847/878
$C_{33}^{T/S}$	649/663	591/615	545/580	933/945	821/850
$C_{12}^{T/S}$	266/280	233/258	222/258	464/477	398/431
$C_{13}^{T/S}$	235/249	218/243	218/256	348/362	324/356
$C_{23}^{T/S}$	251/264	240/265	251/286	383/396	364/395
C_{44}	262	232	202	336	270
C_{55}	219	210	180	266	234
C_{66}	199	178	147	264	195
$K_{T/S}$	382.7/396.8	349.9/375.8	332.7/369.5	565.7/579.4	508.6/542.5
G	214.3	194.9	166.2	269.7	226.9
γ	1.30	1.37	1.40	1.21	1.26
α	1.91	2.15	2.26	1.34	1.51

Here V, a, b, c are unit cell volume and lattice parameters, in Å^3 and Å, respectively; $\sigma_{1,2,3}$ are stress tensor components, showing that non-hydrostatic deviations from the average pressure P are very small; C_{ij} are elastic constants (T, isothermal; S, adiabatic) in GPa (errors of a few per cent); K and G are Voigt-Reuss-Hill bulk and shear moduli in GPa (errors within 2%); γ is the Grüneisen parameter and α thermal expansion in 10^{-5} K^1 (errors within 10%). Important derivatives: $(\partial \ln v_S/\partial T)_P = -3.67 \times 10^{-5}\,K^{-1}$ (38 GPa), $-3.78 \times 10^{-5}\,K^{-1}$ (88 GPa). $(\partial \ln v_P/\partial T)_P = -2.49 \times 10^{-5}\,K^{-1}$ (38 GPa), $-1.98 \times 10^{-5}\,K^{-1}$ (88 GPa). $(\partial \ln v_\Phi/\partial T)_P = -1.65 \times 10^{-5}\,K^{-1}$ (38 GPa), $-0.92 \times 10^{-5}\,K^{-1}$ (88 GPa). $(\partial \ln v_S/\partial \ln v_P)_T = 0.61$ (1,500 K), 0.81 (3,500 K). $(\partial \ln v_S/\partial \ln v_P)_P = 1.48$ (38 GPa), 1.91 (88 GPa). All errors are within 20%.

values, obtained taking full account of anharmonic effects, are still lower than the observed values. Karki *et al.*[17], using the quasiharmonic approximation, found R_P of MgO to increase from 1.4 to 1.9 from the top to the bottom of the lower mantle. This agrees well with our results for $MgSiO_3$; the remaining deficit of R_P can only be explained by either significant anelasticity[4] or large-scale compositional heterogeneity of the lower mantle.

Seismic tomography is a quickly developing technique; the most recent tomography maps have similar qualitative features (locations of cold slabs and hot plumes), and give the absolute velocity perturbations within ~25% uncertainty. For interpreting seismic tomography in terms of temperature, it is most convenient to use the bulk sound velocity v_ϕ, whose seismological determination is unaffected by anelastic effects. The bulk velocity maps can be accurately determined by the joint inversion of the shear and compressional velocities. Perhaps the most reliable global seismic tomography maps currently available are those of Masters *et al.*[5]. Older higher-resolution maps of Kennett *et al.*[18] realistically give much narrower cold (high-velocity) zones, but strongly underestimate the amplitudes of the velocity variations.

We find the temperature derivative of the bulk velocity, $\phi = (\partial \ln v_\phi/\partial T)_P$, to vary from $-1.7 \times 10^{-5}\,K^{-1}$ at 1,000 km to $-0.9 \times 10^{-5}\,K^{-1}$ (errors ±20%) at 2,000 km depth. Temperature variations can be obtained from the relative velocity perturbations: $\delta T = (\delta v_\phi/v_\phi)/\phi$. Combined with bulk sound velocity maps of Masters *et al.*[5] (with maximum velocity contrast $\Delta v_\phi/v_\phi = 1.4\%$ at 1,225 km and 2,195 km), this gives the temperature contrast between the hot plumes and cold slabs increasing from 800 K to 1,500 K between 1,000 and 2,000 km depth. Linear extrapolation gives ~550 K at the top of the lower mantle, and 2,150 K at the bottom. The root-mean-square temperature variations are ~150–250 K across the lower mantle. Our temperature contrasts are ~2–4 times smaller than estimates[19] obtained using extremely uncertain extrapolations of $s = (\partial \ln v_S/\partial T)_P$ and which would suggest partial melting of the lower mantle. Our results can support partial melting only in the lowermost part of the lower mantle. Castle *et al.*[20], using their shear velocity maps for the bottom of the lower mantle (maximum $\Delta v_s/v_s = 7.4\%$) and a reasonable guess for s, obtained an estimate of the temperature contrast at the core–mantle boundary similar to ours, ~1,600 K. Using the v_ϕ-maps of Kennett *et al.*[18] (maximum $\Delta v_s/v_s = 1.0\%$ at 1,225 km and 2,195 km), we get much smaller temperature contrasts, rising from ~500 K to ~1,000 K between the depths of 1,000 km and 2,000 km.

It is becoming increasingly clear that temperature variations are the main factor determining the perturbations of seismic wave velocities in the lower mantle. Anelasticity can be important for the shear velocities, but is negligible for the bulk velocities. Compositional heterogeneity is significant only near the core–mantle boundary[5]; it can occur due to the chemical reaction[21] between core and mantle, driving Fe from the silicate mantle into the metallic core. Hot plumes, rising from the core–mantle boundary, would then be depleted in Fe. When substituting for Mg, Fe dramatically decreases shear moduli of many silicates and oxides, while the effect on bulk moduli is very small. Hence, even minor regional variations of the Fe content can have a major effect on the shear velocities, being less important for the bulk velocity. For example, very hot, slightly Fe-depleted mantle rocks can have the same shear velocities as very cold, slightly Fe-enriched mantle rocks. Consistent with the depletion of plumes in Fe, we find the temperature contrasts at 2,000 km determined for the shear velocities[5,18] (1,000 K from maps[5]) to be smaller than those determined from the corresponding bulk velocities (1,500 K from maps[5]). This effect can even produce an anticorrelation between the bulk and shear velocities, but not its observed[5] pattern: it remains a mystery why it is the bulk (not shear) velocity anomalies that undergo a reversal near the core–mantle boundary (that is, low-velocity zones at the core–mantle boundary underlay high-velocity anomalies of the rest of the lower mantle). In any case, the temperature contrasts obtained from the bulk velocities must be the most reliable, at least outside the anomalous core–mantle boundary region, in which compositional effects seem to be significant for all types of seismic waves. The temperature contrasts that we have found could be used as important constraints in numerical modelling of mantle convection.

Kesson *et al.*[22] estimated that lithospheric slabs should be at least ~650 K colder than surrounding mantle if they are to sink to the core–mantle boundary, and at least 250 K colder to reach the depth of 1,100 km. Our maximum cold temperature anomalies (roughly half of the total temperature contrasts) are similar to these estimates, and suggest that some lithospheric slabs might stop sinking before reaching the core–mantle boundary. Neutrally buoyant slabs would be dissolved by the convecting mantle; some tomographic maps show most slabs disappearing in the middle of the lower mantle[18], while others[5] show that most slabs do reach the core–mantle boundary.

The next step is to estimate the extent of chemical heterogeneity and anelasticity in the lower mantle, and construct a three-dimensional mineralogical model of the Earth's mantle. With improved seismic tomography models and mineral physics data, this could be achieved in the foreseeable future. We believe that *ab initio* molecular dynamics simulations will be important in solving this and many other geologically important problems. □

Received 21 September 2000; accepted 30 April 2001.

1. Anderson, D. L. *Theory of the Earth* (Blackwell Scientific Publications, Boston, 1989).
2. Car, R. & Parrinello, M. Unified approach for molecular dynamics and density-functional theory. *Phys. Rev. Lett.* **55,** 2471–2474 (1985).
3. Kresse, G. & Furthmuller, J. Efficiency of ab initio total-energy calculations for metals and semiconductors using a plane-wave basis set. *Comp. Mater. Sci.* **6,** 15–50 (1996).
4. Karato, S.-i. Importance of anelasticity in the interpretation of seismic tomography. *Geophys. Res. Lett.* **20,** 1623–1626 (1993).
5. Masters, G., Laske, G., Bolton, H. & Dziewonski, A. in *Earth's Deep Interior: Mineral Physics and Tomography From the Atomic to the Global Scale* (eds Karato, S.-i. *et al.*) 63–87 (AGU Geophys. Monogr. 113, American Geophysical Union, Washington DC, 2000).
6. Ancilotto, F., Chiarotti, G. L., Scandolo, S. & Tosatti, E. Dissociation of methane into hydrocarbons at extreme (planetary) pressure and temperature. *Science* **275,** 1288–1290 (1997).
7. Cavazzoni, C. *et al.* Superionic and metallic states of water and ammonia at giant planet conditions. *Science* **283,** 44–46 (1999).
8. Alfé, D., Gillan, M. J. & Price, G. D. The melting curve of iron at the pressures of the Earth's core from *ab initio* calculations. *Nature* **401,** 462–464 (1999).
9. Sugino, O. & Car, R. Ab initio molecular dynamics study of first-order phase transitions: melting of silicon. *Phys. Rev. Lett.* **74,** 1823–1826 (1995).
10. Buda, F., Car, R. & Parrinello, M. Thermal expansion of c-Si via ab initio molecular dynamics. *Phys. Rev. B* **41,** 1680–1683 (1990).
11. da Silva, C., Wentzcovitch, R. M., Patel, A., Price, G. D. & Karato, S.-i. The composition and geotherm of the lower mantle: constraints from the elasticity of silicate perovskite. *Phys. Earth Planet. Inter.* **118,** 103–109 (2000).
12. O'Keeffe, M. & Bovin, J. O. Solid electrolyte behavior of $NaMgF_3$: geophysical implications. *Science* **206,** 599–600 (1979).
13. Matsui, M. & Price, G. D. Simulation of the pre-melting behaviour of $MgSiO_3$ perovskite at high pressures and temperatures. *Nature* **351,** 735–737 (1991).
14. Oganov, A. R., Brodholt, J. P. & Price, G. D. *Ab initio* elasticity and thermal equation of state of $MgSiO_3$ perovskite. *Earth Planet. Sci. Lett.* **184,** 555–560 (2001).
15. Robertson, G. S. & Woodhouse, J. H. Constraints on lower mantle properties from seismology and mineral physics. *Earth Planet. Sci. Lett.* **143,** 197–205 (1996).
16. Shen, G. & Lazor, P. Measurement of melting temperatures of some minerals under lower-mantle pressure. *J. Geophys. Res.* **100,** 17699–17713 (1995).
17. Karki, B. B., Wentzcovitch, R. M., de Gironcoli, S. & Baroni, S. First-principles determination of elastic anisotropy and wave velocities of MgO at lower mantle conditions. *Science* **286,** 1705–1707 (1999).
18. Kennett, B. L. N., Widiyantoro, S. & van der Hilst, R. D. Joint seismic tomography for bulk sound and shear wave speed in the Earth's mantle. *J. Geophys. Res.* **103,** 12469–12493 (1998).
19. Yuen, D. A., Čadek, O., Chopelas, A. & Matyska, C. Geophysical inferences of thermal-chemical structures in the lower mantle. *Geophys. Res. Lett.* **20,** 899–902 (1993).
20. Castle, J. C., Creager, K. C., Winchester, J. P. & van der Hilst, R. D. Shear wave speeds at the base of the mantle. *J. Geophys. Res.* **105,** 21543–21557 (2000).
21. Knittle, E. & Jeanloz, R. Earth's core-mantle boundary: results of experiments at high pressures and temperatures. *Science* **251,** 1438–1443 (1991).
22. Kesson, S. E., Fitz Gerald, J. D. & Shelley, J. M. Mineralogy and dynamics of a pyrolite mantle. *Nature* **393,** 252–255 (1998).
23. Hohenberg, P. & Kohn, W. Inhomogeneous electron gas. *Phys. Rev.* **136,** B864–B871 (1964).
24. Kohn, W. & Sham, L. J. Self-consistent equations including exchange and correlation effects. *Phys. Rev.* **140,** A1133–A1138 (1965).
25. Wang, Y. & Perdew, J. P. Correlation hole of the spin-polarized electron gas, with exact small-vector and high-density scaling. *Phys. Rev. B* **44,** 13298–13307 (1991).

26. Nosé, S. A molecular dynamics method for simulations in the canonical ensemble. *Mol. Phys.* **52,** 255–268 (1984).
27. Wallace, D. C. *Thermodynamics of Crystals* (Dover Publications, New York, 1998).

Acknowledgements

We acknowledge receipt of a Russian President Scholarship for Education Abroad, a UCL Graduate School Research Scholarship, and a UK Overseas Research Scholarship (A.R.O.) and a Royal Society University Research Fellowship (J.P.B.). We thank NERC for access to the supercomputer facilities.

Correspondence and requests for materials should be addressed to A.R.O. (e-mail: a.oganov@ucl.ac.uk).

Major fungal lineages are derived from lichen symbiotic ancestors

François Lutzoni*†, Mark Pagel‡ & Valérie Reeb*†§

* *Department of Botany, The Field Museum of Natural History, 1400 South Lake Shore Drive, Chicago, Illinois 60605, USA*
‡ *School of Animal and Microbial Sciences, University of Reading, Whiteknights, Reading RG6 6AJ, UK*
§ *Department of Biological Sciences, University of Illinois at Chicago (M/C 066), Chicago, Illinois 60607, USA*

About one-fifth of all known extant fungal species form obligate symbiotic associations with green algae, cyanobacteria or with both photobionts. These symbioses, known as lichens, are one way for fungi to meet their requirement for carbohydrates[1,2]. Lichens are widely believed to have arisen independently on several occasions, accounting for the high diversity and mixed occurrence of lichenized and non-lichenized (42 and 58%, respectively) fungal species within the Ascomycota[3,4]. Depending on the taxonomic classification chosen[2,5,6], 15–18 orders of the Ascomycota include lichen-forming taxa, and 8–11 of these orders (representing about 60% of the Ascomycota species) contain both lichenized and non-lichenized species. Here we report a phylogenetic comparative analysis of the Ascomycota, a phylum that includes greater than 98% of known lichenized fungal species[5]. Using a Bayesian phylogenetic tree sampling methodology[7,8] combined with a statistical model of trait evolution[9], we take into account uncertainty about the phylogenetic tree and ancestral state reconstructions. Our results show that lichens evolved earlier than believed, and that gains of lichenization have been infrequent during Ascomycota evolution, but have been followed by multiple independent losses of the lichen symbiosis. As a consequence, major Ascomycota lineages of exclusively non-lichen-forming species are derived from lichen-forming ancestors. These species include taxa with important benefits and detriments to humans, such as *Penicillium* and *Aspergillus*[10–12].

To investigate the evolution of the lichen symbiosis it is necessary to account for the phylogenetic relationships within the Ascomycota, and to infer the rates and likely pattern of gains and losses of the symbiotic state. We reduced the high level of uncertainty associated with small subunit nuclear ribosomal RNA gene (SSU nuclear rDNA) phylogenies of the Ascomycota[13–15], by obtaining sequences from the small and large subunit (LSU) of the nuclear rRNA genes for 52 species of the Ascomycota. Our sample includes representatives from 24 of 46 orders[2], representing ≈75% of the Ascomycota species diversity.

Phylogenetic comparative investigations typically rely on a single phylogenetic tree and reconstruct ancestral states on the basis of the method of parsimony. However, phylogenetic trees are rarely known without error and different tree topologies can give different estimates of ancestral states. In addition, ancestral states reconstructed by parsimony do not account for the statistical uncertainty of ancestral inferences. Both of these problems are acute when reconstructing the evolution of the lichen symbiosis. All previous broad phylogenetic studies of the Ascomycota had low bootstrap support and unstable relationships in critical portions of the trees[4,12–17]. Furthermore, parsimony methods may perform poorly when rates of character evolution are high[18,19].

We used a Bayesian statistical procedure based on Markov chain Monte Carlo (MCMC) sampling methods[7] to account for phylogenetic uncertainty. This sampling procedure allows us to draw a random sample from the universe of possible phylogenetic trees. The frequency distribution of the sample estimates the posterior probability distribution of trees (see Methods). From the distribution of sampled trees we calculated the posterior probability of ancestral nodes and focused our data interpretation on those nodes with the highest statistical certainty.

We used a statistical model of trait evolution[9,20,21] to estimate on each tree the evolutionary rate of gains and losses of lichenization, and the most probable ancestral states (lichen-forming/non-lichen-forming) at specified nodes. Rates of evolution between states are calculated over all possible states at each node of a given tree and are therefore independent of any particular reconstruction of the ancestral states. The model of trait evolution takes into account the lengths of the branches of the phylogenetic tree, does not constrain the rates of gains and losses *a priori*, and expresses the statistical uncertainty associated with estimates of ancestral states at each node. To derive an overall estimate of the rates of evolution or the probability of an ancestral state, the estimates from each tree are averaged (see Methods). Our inferences about the nature of the evolutionary processes underlying lichen evolution thereby take account of uncertainty inherent to the phylogenetic hypothesis, and are not conditional on any particular tree.

We sampled 19,900 phylogenetic trees using the MCMC procedure[7], and estimated by maximum likelihood the rates of gains and losses of lichenization on each (Fig. 1). Larger rate values correspond to a higher expected number of transformations (losses or gains), and the loss/gain ratio (dots in Fig. 1) directly estimates the ratio of expected losses to expected gains of lichenization during evolution.

In contrast with previous work on the evolution of the lichen symbiosis[4], our results show that rates of loss of lichenization exceed rates of gain in the Ascomycota. In 18,029 of the 19,900 sampled trees (90.6%) the estimated rate of loss exceeds the rate of gain (that is, the loss/gain ratio is greater than one, and therefore is above the

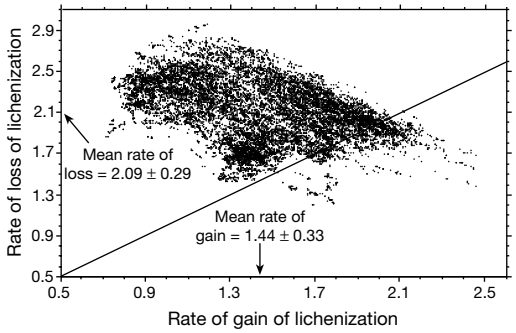

Figure 1 The rate of loss of lichenization exceeds the rate of gain of lichenization, independently of tree topology. Data are for 19,900 MCMC trees. The 1:1 relationship is indicated by the solid line.

† Present address: Department of Biology, Duke University, Durham, North Carolina 27708, USA.